Observation of indirect ionization of W^{7+} in an electron-beam ion-trap plasma

Q. Lu,[1,2] J. He,[1,2] H. Tian,[1,2] M. Li,[1,2] Y. Yang,[1,2] K. Yao,[1,2] C. Chen,[1,2] J. Xiao,[1,2,*] J. G. Li,[3,†] B. Tu,[4,‡] and Y. Zou[1,2]

[1]*Institute of Modern Physics, Department of Nuclear Science and Technology, Fudan University, Shanghai 200433, China*

[2]*Key Laboratory of Nuclear Physics and Ion-Beam Application (MOE), Fudan University, Shanghai 200433, China*

[3]*Institute of Applied Physics and Computational Mathematics, Beijing 100088, China*

[4]*Max-Planck-Institut für Kernphysik, Saupfercheckweg 1, 69117 Heidelberg, Germany*

(Received 8 January 2019; published 19 April 2019)

In this work, visible and extreme ultraviolet spectra of W^{7+} are measured using the high-temperature superconducting electron-beam ion trap (EBIT) at the Shanghai EBIT Laboratory under extremely low-energy conditions (lower than the nominal electron-beam energy of 130 eV). The relevant atomic structure is calculated using the flexible atomic code package based on the relativistic configuration interaction method. The GRASP2K code, in the framework of the multiconfiguration Dirac-Hartree-Fock method, is employed as well for calculating the wavelength of the $M1$ transition in the ground configuration of W^{7+}. A line from the W^{7+} ions is observed at a little higher electron-beam energy than the ionization potential for W^{4+}, making this line appear to be from W^{5+}. A hypothesis for the charge-state evolution of W^{7+} is proposed based on our experimental and theoretical results; that is, the occurrence of W^{7+} ions results from indirect ionization caused by stepwise excitation between some metastable states of lower-charge-state W ions, at the nominal electron-beam energy of 59 eV.

DOI: 10.1103/PhysRevA.99.042510

I. INTRODUCTION

As the metal with the highest melting point, tungsten is considered to be the optimal candidate for wall material of divertors in tokamaks because of its numerous superb properties [1,2]. However, plasma-wall interactions would make tungsten pass into the core plasma as impurities, which may finally lead to the flameout of fusion [3]. Moreover, radiation from tungsten ions could carry information about the plasma state, and thus it is essential to obtain and analyze the spectra of tungsten. Since an electron-beam ion trap (EBIT) employs a quasimonoenergetic and energy-adjustable electron beam to ionize trapped ions, and is capable of providing specific ions with any targeted charge state, it has been proved to be a good tool for use in disentanglement studies of atomic processes in plasmas in recent years [4].

To date, many studies have been carried out on highly charged tungsten ions related to the core plasma in tokamaks since the corresponding atomic systems are relatively simple [5–17]. With respect to lowly charged tungsten ions (W^{+}–W^{13+}) existing in edge plasma, their more complex atomic structures due to the number of electrons, especially the open $4f$ subshell and competition of orbital energies between $4f$ and $5p$ electrons, result in the difficulty of theoretical calculation [18] and in line identification.

With development of the low-energy EBIT, some progress has been made on the atomic spectra for lowly charged tungsten ions. For example, spectra of W^{11+}–W^{15+} in the (17–26)-nm region were measured and analyzed by Li *et al.* [19]. Moreover, Li *et al.* found a strong visible line from W^{11+} [20]. Experiments on W^{13+} were conducted by different EBIT groups as well [21,22]. For W^{8+}–W^{12+} ions, however, spectral data are still rare. In addition to EBIT plasma, numerous works on lowly charged tungsten ions have been done in vacuum spark plasma [23–30].

It can be seen from Ref. [31] that the ionization energy of W^{6+} ions (122.01 ± 0.06 eV) is much larger than that of W^{5+} ions (64.77 ± 0.04 eV). The opening of the $4f$ subshell ($4f^{13}\,5s^{2}\,5p^{6}$) may account for this large gap in ionization energy, and has attracted extensive attention to W^{7+} ions. For example, experiments on W^{5+}–W^{7+} in the extreme ultraviolet (EUV) range were conducted at Livermore EBIT Laboratory [32]. Mita *et al.* reported their direct observation of the $M1$ transition between the fine structure belonging to the ground configuration of W^{7+} ions [33]. According to their results, the $M1$ line appeared in advance compared with theoretical ionization energy of 122 eV. Therefore, Mita *et al.* proposed that the occurrence of W^{7+} may arise from ionization through the metastable excited states of lower-charged tungsten ions. However, this hypothesis has not been confirmed yet.

As for this indirect ionization process, i.e., ionization via one or more intermediate metastable levels, there exist some relevant reports. For example, the occurrence of Sn^{11+}–Sn^{14+} below ionization energy was found by Windberger *et al.* [34]. Sakoda *et al.* proposed that Ba^{11+} could appear earlier than expected through indirect ionization from the metastable state of Ba^{10+} [35]. Moreover, Qiu *et al.* discovered some excited metastable states with extraordinarily high population in W^{28+} [36]. However, more systematic, quantitative studies into the role of indirect ionization in the charge-state evolution of heavy species such as W need to be done.

In this work, the spectra of W^{7+} ions in the visible and EUV ranges are measured at the high-temperature

*xiao_jun@fudan.edu.cn

†Li_Jiguang@iapcm.ac.cn

‡bingsheng.tu@mpi-hd.mpg.de

superconducting electron-beam ion trap (SH-HtscEBIT) [37]. The atomic structures of W^{5+}, W^{6+}, and W^{7+} are calculated using the relativistic configuration interaction (RCI) method implemented in the FLEXIBLE ATOMIC CODE (FAC) package [38,39]. In addition, the GRASP2K code [40,41], based on multiconfiguration Dirac-Hartree-Fock theory, is also employed to calculate the energy structure.

II. EXPERIMENTAL SETUP

Our experiment is conducted using the SH-HtscEBIT, specially designed for providing atomic data for fusion-edge plasma research [19,37]. This EBIT is capable of operating in the range of electron-beam energies between 30 and 4000 eV, and it is therefore able to create tungsten ions, for example, of charge states from around 2+ to below 46+. The magnetic field, which is created by superconducting coils operating at liquid-nitrogen temperature, compresses the beam radius to 150 μm. The background vacuum pressure in the trap center is estimated to be lower than 1.0×10^{-9} Torr, which minimizes the effect on the tungsten charge-state distribution. Basically each new charge state is formed at the ionization energy of the previous one, giving an important aid in spectral line identification.

The tungsten ions used in the present work are obtained by continuously injecting $W(CO)_6$ gas, which has a very low sublimation point at atmospheric pressure. Once the $W(CO)_6$ molecules enter the region of the central drift tube, they are quickly destroyed. Monoenergetic beam electrons collide with injected atoms to form a thin plasma. Ions at the center of the drift tube are confined axially by the potential well (100 V) and radially by the space-charge effect of electrons and the magnetic field. The trapped ions are collided with the electron beam emitted from a LaB6 cathode and accelerated by the potential difference between the central drift tube and the cathode. Finally, photon radiation from excited states is detected by an Andor Shamrock 303 spectrometer for visible range and a grazing-incidence flat-field spectrometer for the EUV range [42].

III. THEORETICAL CALCULATION

An integrated software package (FAC) is used in this work, which can produce atomic structure, such as energy levels, transition rates, and collision (de)excitation rates [14,38,39].

To simulate spectra under different plasma conditions, a collisional-radiative model (CRM) implemented in FAC is adopted [43,44]. Here, a balanced system is established in CRM to obtain the energy-level population. In the environment of the low-energy EBIT, three main dynamic processes involving electron-impact excitation, electron-impact deexcitation, and radiative decay are included, while other processes such as charge exchange and radiative recombination are ignored. On the basis of this assumption, the differential rate of the population of each energy level can be expressed as

$$\frac{dN_i}{dt} = \sum_{j>i} \left(A^r_{j\to i} N_j\right) + \sum_{j<i} \left(C^e_{j\to i} N_j\right) + \sum_{j>i} \left(C^d_{j\to i} N_j\right) - \sum_{j<i} \left(A^r_{i\to j} N_i\right) - \sum_{j>i} \left(C^e_{i\to j} N_i\right) - \sum_{j<i} \left(C^d_{i\to j} N_i\right),$$

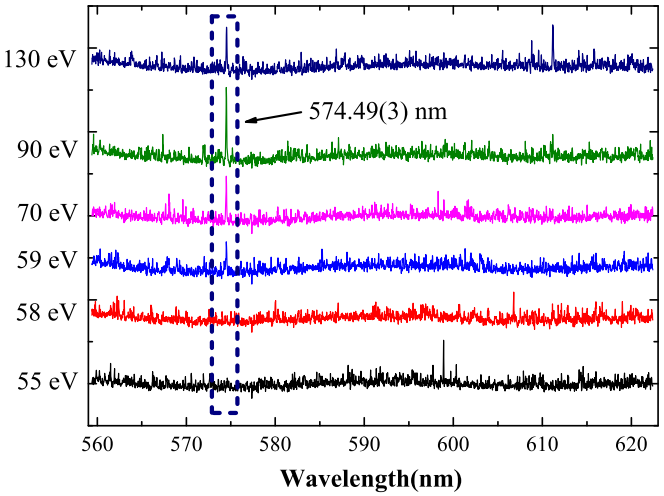

FIG. 1. Spectra of tungsten obtained by SH-HtscEBIT at nominal electron-beam energies of 55, 58, 59, 70, 90, and 130 eV in the range 559–623 nm. Accumulation time of each spectrum is 2 h. Line at 574.49(3) nm is the $M1$ transition between the fine-structure levels in the $4f^{13}\,5s^2\,5p^6\,{}^2F$ ground term of W^{7+}.

where N is the population number, the subscripts (i, j) represent the initial or the final energy levels, and A^r, C^e, and C^d stand for the radiative decay rate, electron-impact excitation rate, and electron-impact deexcitation rate, respectively. Considering the equilibrium condition $\frac{dN_i}{dt} = 0$ and the normalized condition $\sum_i N_i = 1$, we can solve the equation above and further obtain the population of each energy level.

The line intensity can be calculated, once level populations and transition rates are given. The simulated spectra are presented with wavelength (given by RCI) and intensity (given by CRM) for analyzing the experimental spectra.

IV. RESULTS AND DISCUSSION

A. Visible line of W^{7+}

Spectra in the range 559–623 nm from tungsten ions, which are obtained at the nominal electron-beam energies of 55, 58, 59, 70, 90, and 130 eV, are shown in Fig. 1.

The line at 574.49(3) nm just appears when the nominal electron-beam energy is tuned from 58 to 59 eV, indicating that a new charge state is created. We also find a dependence of the line intensity on the electron-beam energy, which becomes maximum at nearly 90 eV, and decreases as the energy is at 130 eV.

Since the nominal electron-beam energy represents only the voltage difference between the cathode and central drift tube DT2, the real electron-beam energy must be corrected from that. Usually, the electron-beam energy can be given in the following expression [45]:

$$E_{\rm corr}[\rm eV] = e\{V_{\rm DT2}[\rm V] - V_{\rm Cathode}[\rm V] + V_{\rm sp}[\rm V]\},$$

where $E_{\rm corr}$ is the real electron-beam energy, $V_{\rm DT2}$ the voltage of DT2, $V_{\rm Cathode}$ the voltage of the cathode, and $V_{\rm sp}$ the potential produced by space charges.

The correction of the electron-beam energy is divided into two parts. The first part is the power-supply correction, which is a deviation between the set value and output value of

TABLE I. Correction of electron-beam energies: set potential difference between cathode and DT2 (nominal electron-beam energy), $E_{\rm set}$; output potential difference between cathode and DT2, $E_{\rm out}$; space charge effect from electrons and ions, $V_{\rm sp}$; and finally corrected electron-beam energy, $E_{\rm corr}$. Uncertainties for $V_{\rm sp}$ and $E_{\rm corr}$ are also given.

$E_{\rm set}$ (eV)	$E_{\rm out}$ (eV)	$V_{\rm sp}$ (eV)	$E_{\rm corr}$ (eV)
58.0	64.4	13.4 ± 2.5	51.0 ± 2.5
59.0	65.4	10.5 ± 2.1	54.9 ± 2.1

the power supplies. One multimeter (Fluke 17B) is used to measure the actual output voltage, and the results are listed in Table I.

The second part is the correction from the space-charge effect. The space-charge effect $V_{\rm sp}$, which is typically dozens of eV, results in the reduction of electron-beam energy. In case of lowly-charged tungsten ions, the ionization energy interval of adjacent charged ions is comparable to $V_{\rm sp}$, and thus confuses the charge-state identification. The space-charge effect can be estimated by [46]

$$V_{{\rm sp},n}[{\rm V}] = \frac{30 I_e[{\rm A}]}{\sqrt{1-\left(\frac{E_{\rm set}-eV_{{\rm sp},n-1}}{511\,000}[{\rm eV}]+1\right)^{-2}}}\left[\ln\left(\frac{r_e}{r_{\rm dt}}\right)^2 - 1\right]$$

In the equation above, $V_{{\rm sp},n}$ is the convergent space-charge potential after the nth iteration; I_e (2–3 mA in this case) represents the value of the electron-beam current; $E_{\rm set}$ is the potential difference between the DT2 and cathode; r_e denotes the radius of the electron beam, typically 150 μm; and $r_{\rm dt}$, 1 mm, labels the radius of the drift tube.

In addition to electrons, ions also have a space-charge effect, which compensates for the influence of electrons. Here a coefficient of 0.4 is introduced based on the results in Ref. [46], in which the experimental conditions are very similar to ours. It should be noted that this coefficient may introduce an uncertainty of approximately 10% in this case. The corrected electron-beam energy and the uncertainties are displayed in Table I. The ionization energy of tungsten is listed in Table II.

Based on the relation between the corrected electron-beam energy and tungsten ionization energy, the line at 574.49 nm appears as long as the electron-beam energy exceeds the ionization energy of W^{4+}, i.e., 51.6 eV, rather than W^{6+}. The experimental results indicate that the line at 574.49 nm could not come from W^{7+}; rather it comes from those of charge states under 7+. To identify this line, the RCI method in the FAC package is used to calculate the atomic structure of W^{5+}, W^{6+}, and W^{7+}. Part of their energy levels is shown in Figs. 2, 3, and 4, respectively.

TABLE II. Ionization energies of tungsten [31].

Ion charge	Ionization energy (eV)
+3	38.2 ± 0.4
+4	51.6 ± 0.3
+5	64.77 ± 0.04
+6	122.01 ± 0.06

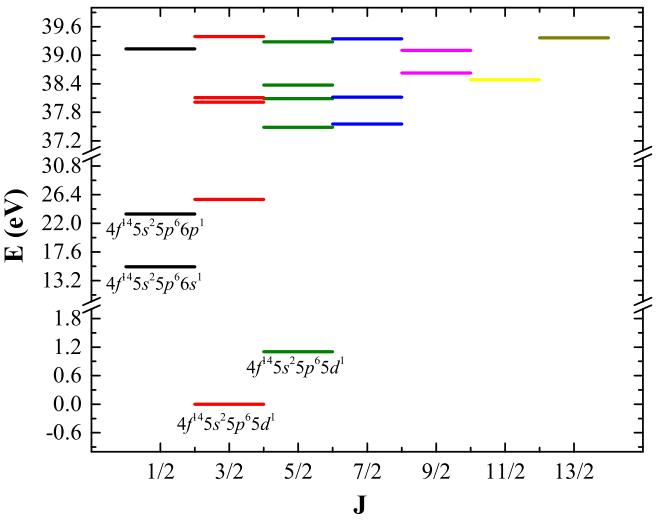

FIG. 2. Partial energy-level diagram of W^{5+} with the lowest (in energy) 20 energy levels from the flexible atomic code calculations.

According to the calculations, lines from W^{5+} ions with strong intensity are not in the visible range, but in the EUV range instead. The strong M1 transition line $^2D_{5/2} - {}^2D_{3/2}$ in the ground configuration $4f^{14}\,5s^2\,5p^6\,5d^1$ lies in the infrared range.

The ground state of W^{6+} is $4f^{14}\,5s^2\,5p^6\ {}^1S_0$, and there is no fine-structure splitting. Several $M1$ transition lines near 500 nm with relatively large strengths belonging to the first-excited configuration $4f^{14}\,5s^2\,5p^5\,5d^1$ are estimated by CRM. Note that the simulated strengths of these lines are almost

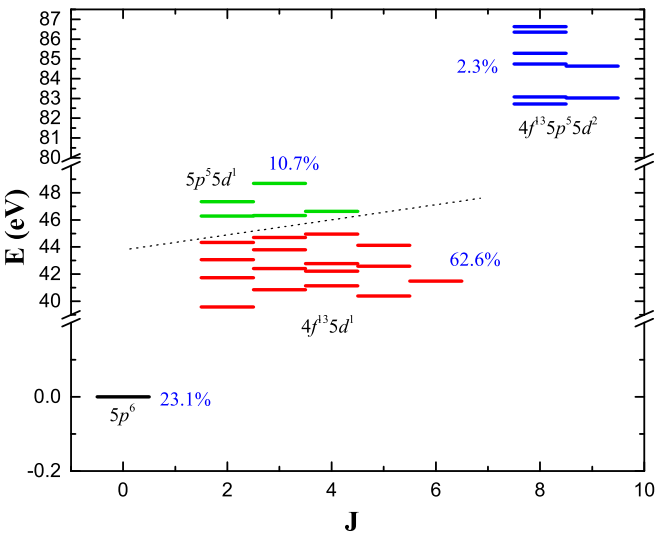

FIG. 3. Partial energy-level diagram of W^{6+} including energy levels with relatively high population. Shown are one energy level belonging to the $4f^{14}\,5s^2\,5p^6$ configuration (black), 16 energy levels belonging to the $4f^{13}\,5s^2\,5p^6\,5d^1$ configuration (red), five energy levels belonging to the $4f^{14}\,5s^2\,5p^5\,5d^1$ configuration (green), and eight energy levels belonging to the $4f^{13}\,5s^2\,5p^5\,5d^2$ configuration (blue). Total populations of each configuration are marked with blue numbers, which are calculated by FAC at electron-beam energy 55 eV and density $1.0 \times 10^{11}/{\rm cm}^3$.

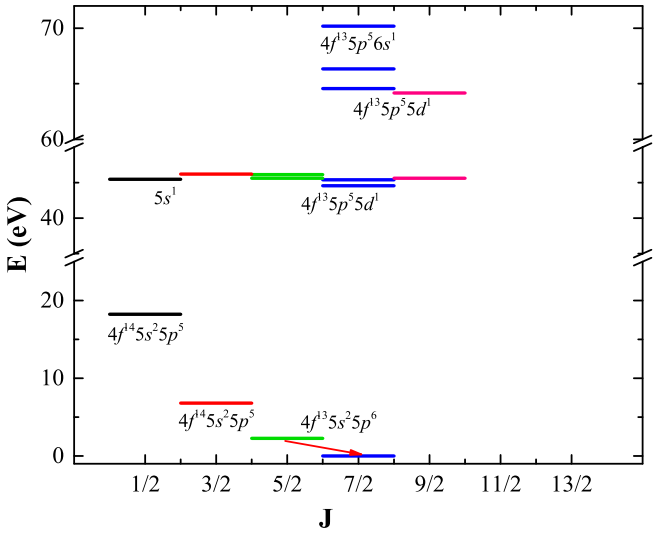

FIG. 4. Partial energy-level diagram of W^{7+} with lowest (in energy) 15 energy levels from FAC calculations. The red arrow represents the $M1$ transition between the ground configuration $4f^{13}\,5s^2\,5p^6$.

the same. However, no lines near 500 nm are observed in the present experiment.

Finally, the theoretical wavelength, 548.61 nm, computed by the FAC code shows that the $M1$ transition in the ground configuration $4f^{13}\,5s^2\,5p^6\ {}^2F_{5/2} - {}^2F_{7/2}$ of W^{7+} is the only strong transition in the visible range (see Fig. 4). This value is consistent with that calculated by Berengut *et al.* (549.55 nm) [47]. However, Kramida *et al.* [48] evaluated this splitting to be 573.4 nm empirically from the measured $J = 5/2 - J = 7/2$ separation of the $4f^{13}\ 6s$, $7s$, $6p$, and $5f$ levels of W^{6+}. It is worth noting that this result is in excellent agreement with the present experimental value.

Considering that the discrepancy in the wavelength between the FAC calculation (548.61 nm) and the experimental value (574.49 nm) is 4.50%, we have made a multiconfiguration Dirac-Hartree-Fock (MCDHF) calculation using the GRASP code [40,41] to verify the source of this line.

In the MCDHF calculation, the active space approach is adopted to capture the main electron correlations. The correlation among the $5s$, $5p$, and $4f$ valence electrons and the correlation between the $4s$, $4p$, $4d$, and $n = 3$ in the core and the outer valence electrons are taken into account by the configuration-state functions generated through restricted single (S) and double (D) excitations from the

TABLE III. Fine-structure splitting (in cm^{-1}) and corresponding $M1$ transition wavelength (in nm) calculated by using the multiconfiguration Dirac-Hartree-Fock method. Breit and QED represent Breit interaction and quantum electrodynamical effects, respectively.

Models	Transition energy (cm^{-1})	Wavelength (nm)
DF	178 99	558.69
MCDHF	181 28	551.63
Breit	174 25	573.89
QED and Breit	174 35	573.56

TABLE IV. Comparison of experimental and theoretical results of $M1$ transition in ground term $4f^{13}\,5s^2\,5p^6\ {}^2F$ from W^{7+}.

Name	Year	Type	Wavelength (nm)
Ryabtsev *et al.* [49]	2015	Expt.	574.46(16)
Mita *et al.* [33]	2016	Expt.	574.47(3)
This work	2018	Expt.	574.49(3)
Kramida and Shirai [48]	2009	Theor.	573.47
Berengut *et al.* [47]	2009	Theor.	549.55
This work (by FAC)	2018	Theor.	548.61
This work (by GRASP)	2018	Theor.	573.56

$3s^2\,3p^6\,3d^{10}\,4s^2\,4p^6\,4d^{10}\,4f^{13}\,5s^2\,5p^6$ ground configuration to a virtual orbital set. The restriction means that only one out of $n = 3$, $4s$, $4p$, and $4d$ core orbitals can be replaced by the virtual orbitals each time. The set of virtual orbitals is augmented layer by layer, and each layer is composed of orbitals with different angular symmetries up to "g" except for the first layer where the "h" orbital is added as well. Four layers of virtual orbitals are required to make the fine-structure splitting converge. As can be seen from Table III, the fine-structure splitting of the $4f^{13}\,5s^2\,5p^6$ ground configuration for W^{7+} is not sensitive to the electron correlation. It is worth noting that the correlations related to the $3s$, $3p$, $3d$, $4s$, $4p$, and $4d$ core electrons are not negligible. They change the fine-structure splitting by approximately 1%. The Breit interaction and quantum electrodynamical (QED) effects are considered in the subsequent relativistic configuration interaction (RCI) computations. We found from Table III that the Breit interaction makes a significant contribution to this fine-structure splitting, which reaches approximately 5%. The wavelength calculated by the GRASP code is in good agreement with our and other experimental values. This confirms that this line corresponds to the $M1$ transition in the ground configuration of W^{7+}. For comparison, the present experimental and theoretical values of the wavelength for this line are listed in Table IV as well as other available results.

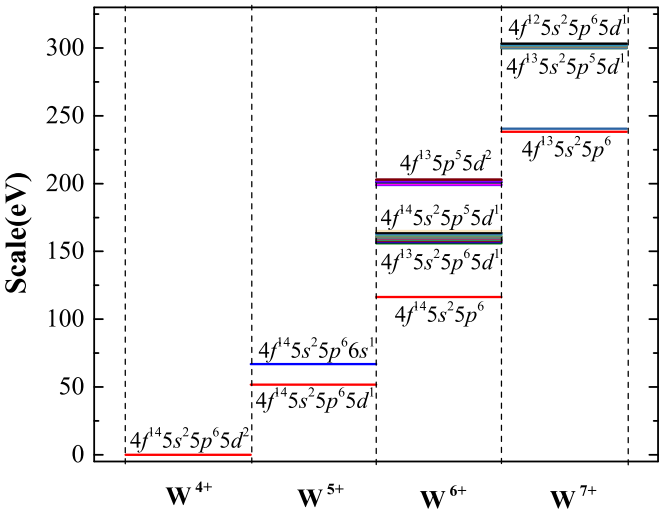

FIG. 5. Hypothesis of charge-state evolution of W^{7+} from W^{4+}. Bold red lines represent the ground level of each charge state, while lines of other colors represent the metastable level.

TABLE V. Information about energy levels taking effect in the indirect ionization process for W^{7+} ions. Energy here represents the relative energy compared to the ground state (0 eV) in each charge state. The computation is conducted at electron-beam energy 55 eV and density $1.0 \times 10^{11}/\mathrm{cm}^3$.

Charge state	Energy level	Energy (eV)	Population (%)	Lifetime (ms)
W^{5+}	$(4f^{14}\,5s^2\,5p^6\,6s^1)_{1/2}$	15.30	0.5	0.02
W^{6+}	$(4f^{13}\,5s^2\,5p^6\,5d^1)_2$	39.57	3.1	0.09
First metastable platform				
	$(4f^{13}\,5s^2\,5p^6\,5d^1)_5$	40.38	7.6	0.09
	$(4f^{13}\,5s^2\,5p^6\,5d^1)_3$	40.83	3.9	0.09
	$(4f^{13}\,5s^2\,5p^6\,5d^1)_4$	41.13	5.4	0.09
	$(4f^{13}\,5s^2\,5p^6\,5d^1)_6$	41.48	8.6	0.10
	$(4f^{13}\,5s^2\,5p^6\,5d^1)_2$	41.74	2.0	0.10
	$(4f^{13}\,5s^2\,5p^6\,5d^1)_4$	42.21	4.4	0.10
	$(4f^{13}\,5s^2\,5p^6\,5d^1)_3$	42.42	3.2	0.09
	$(4f^{13}\,5s^2\,5p^6\,5d^1)_5$	42.58	5.7	0.09
	$(4f^{13}\,5s^2\,5p^6\,5d^1)_4$	42.77	4.0	0.09
	$(4f^{13}\,5s^2\,5p^6\,5d^1)_2$	43.06	1.6	0.09
	$(4f^{13}\,5s^2\,5p^6\,5d^1)_3$	43.80	2.4	0.09
	$(4f^{13}\,5s^2\,5p^6\,5d^1)_5$	44.13	4.1	0.10
	$(4f^{13}\,5s^2\,5p^6\,5d^1)_2$	44.34	1.4	0.10
	$(4f^{13}\,5s^2\,5p^6\,5d^1)_3$	44.70	2.2	0.10
	$(4f^{13}\,5s^2\,5p^6\,5d^1)_4$	44.95	3.0	0.09
	$(4f^{14}\,5s^2\,5p^5\,5d^1)_2$	46.29	1.5	0.11
	$(4f^{14}\,5s^2\,5p^5\,5d^1)_3$	46.32	2.6	0.10
	$(4f^{14}\,5s^2\,5p^5\,5d^1)_4$	46.63	3.1	0.11
	$(4f^{14}\,5s^2\,5p^5\,5d^1)_2$	47.35	1.2	0.11
	$(4f^{14}\,5s^2\,5p^5\,5d^1)_3$	48.69	2.3	0.11
W^{6+}Second metastable platform	$(4f^{13}\,5s^2\,5p^5\,5d^2)_8$	82.72	0.2	0.42
	$(4f^{13}\,5s^2\,5p^5\,5d^2)_9$	83.02	0.4	0.43
	$(4f^{13}\,5s^2\,5p^5\,5d^2)_8$	83.07	0.2	0.44
	$(4f^{13}\,5s^2\,5p^5\,5d^2)_9$	84.64	0.5	0.38
	$(4f^{13}\,5s^2\,5p^5\,5d^2)_8$	84.74	0.3	0.38
	$(4f^{13}\,5s^2\,5p^5\,5d^2)_8$	85.28	0.3	0.42
	$(4f^{13}\,5s^2\,5p^5\,5d^2)_8$	86.35	0.2	0.32
	$(4f^{13}\,5s^2\,5p^5\,5d^2)_8$	86.62	0.2	0.30

The 574.49-nm line from W^{7+} is observed at nominal electron-beam energy setting 59 eV ($E_{\mathrm{corr}} = 54.9$ eV), which exceeds the ionization energy of W^{4+}, i.e., 51.6 eV, but is lower than the ionization energy of W^{5+}, 64.77 eV, and of W^{6+}, 122.01 eV. This means that the visible line from W^{7+} appears two charge states in advance in this experiment. Therefore, a hypothesis of indirect ionization in the charge-state evolution for generating W^{7+} ions can be proposed, as shown in Fig. 5.

A large number of W^{5+} ions are produced through direct ionization from W^{4+}, when the electron-beam energy exceeds the ionization energy 51.6 eV. For the W^{5+} ion, it should be noted that there exists a metastable state $4f^{14}\,5s^2\,5p^6\,6s^1\ {}^2S_{1/2}$, 15.3 eV higher than the ground state $4f^{14}\,5s^2\,5p^6\,5d^1\ {}^2D_{3/2}$, with a relatively high population. This leads to reduction of the ionization energy of W^{5+} from 64.8 to 49.5 eV. Therefore, W^{6+} ions could be yielded through indirect ionization from this metastable state at the same time once W^{5+} ions occur.

According to the FAC calculation, as shown in Fig. 5, there exist two metastable platforms for W^{6+}. The first metastable platform consists of two different configurations, that is, $4f^{13}\,5s^2\,5p^6\,5d^1$ and $4f^{14}\,5s^2\,5p^5\,5d^1$. Configuration $4f^{13}\,5s^2\,5p^6\,5d^1$ has 16 energy levels with 62.6% population in total and configuration $4f^{14}\,5s^2\,5p^5\,5d^1$ contains five en-

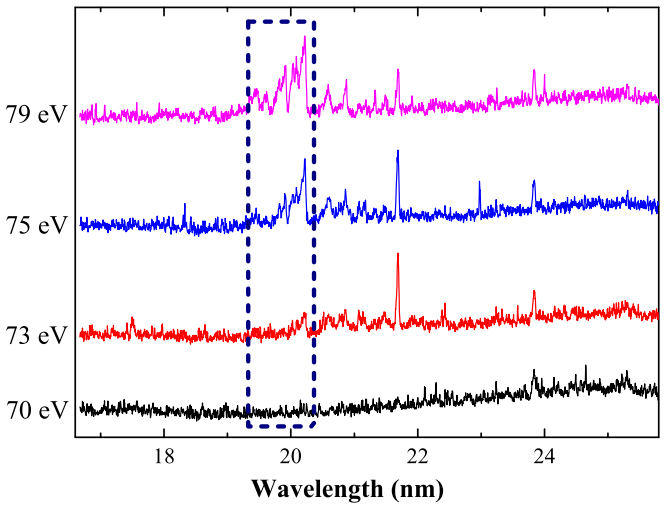

FIG. 6. Spectra of tungsten obtained at SH-HtscEBIT with nominal electron-beam energies 70, 73, 75, and 79 eV in the EUV range 17–26 nm.

TABLE VI. Correction of the electron-beam energy when measuring EUV-range spectra: set potential difference between cathode and DT2 (nominal electron-beam energy), E_{set}; output potential difference between cathode and DT2, E_{out}; space charge effect from electrons and ions, V_{sp}; and finally corrected electron-beam energy E_{corr}. Uncertainties for V_{sp} and E_{corr} are also given.

E_{set} (eV)	E_{out} (eV)	V_{sp} (eV)	E_{corr} (eV)
70.0	77.4	17.4 ± 3.5	60.0 ± 3.5
73.0	80.3	16.4 ± 3.2	63.9 ± 3.2
75.0	82.3	16.1 ± 3.4	65.7 ± 3.4
79.0	86.2	14.3 ± 3.1	71.9 ± 3.1

ergy levels with overall 10.7% population. The average energy of this platform is approximately 44.2 eV higher than the ground state, and less than the electron-beam energy of 54.9 eV, so that the electrons could reach this platform by collision excitation. Moreover, the platform has extremely high population (up to 73%) and long lifetime (on the millisecond order of magnitude). The adequate populations of these metastable states enable further collisional excitations from this platform toward higher energy levels.

The energy of the second platform of metastable states is approximately 40.5 eV higher than the first metastable platform (below the electron-beam energy 54.9 eV), and includes several energy levels belonging to configuration $4f^{13}\,5s^2\,5p^5\,5d^2$. According to Pindzola and Griffin [50], the excitation cross section for the $5p-5d$ transition from configuration $4f^{13}\,5s^2\,5p^6\,5d^1$ of the first metastable platform (62.6% population) to configuration $4f^{13}\,5s^2\,5p^5\,5d^2$ of the second metastable platform is 215.66 Mb, which is much larger than other transitions. Such a large cross section and the high population enhance the possibility for electrons to reach this platform by means of stepwise excitation, and then reach the ground state of W^{7+}, whose energy is 37.3 eV higher. Consequently, W^{7+} ions can be produced in this way.

In short, when the electron-beam energy is tuned from the nominal electron-beam energy setting 58 eV ($E_{corr} = 51.0$ eV) to 59 eV ($E_{corr} = 54.9$ eV), just exceeding the ionization energy of W^{4+} (51.6 eV), a large number of W^{5+} ions is generated by direct ionization. Then, W^{6+} ions are produced through indirect ionization from the metastable state $4f^{14}\,5s^2\,5p^6\,6s^1\ ^2S_{1/2}$ of W^{5+}. In the same way, W^{7+} ions are finally produced by indirect ionization from the second metastable platform ($4f^{13}\,5s^2\,5p^5\,5d^2$) of W^{6+}. As a result, the $M1$ transition line from the W^{7+} ground configuration, located near 574.49 nm, is observed. Energy levels, which play key roles in the indirect ionization process for W^{7+} ions, are shown in Table V.

B. EUV spectra of W^{7+}

The spectra from the W^{7+} ions in the EUV ranging from 17 to 26 nm are measured under nominal electron-beam energies of 70, 73, 75, and 79 eV, respectively. The measurement time

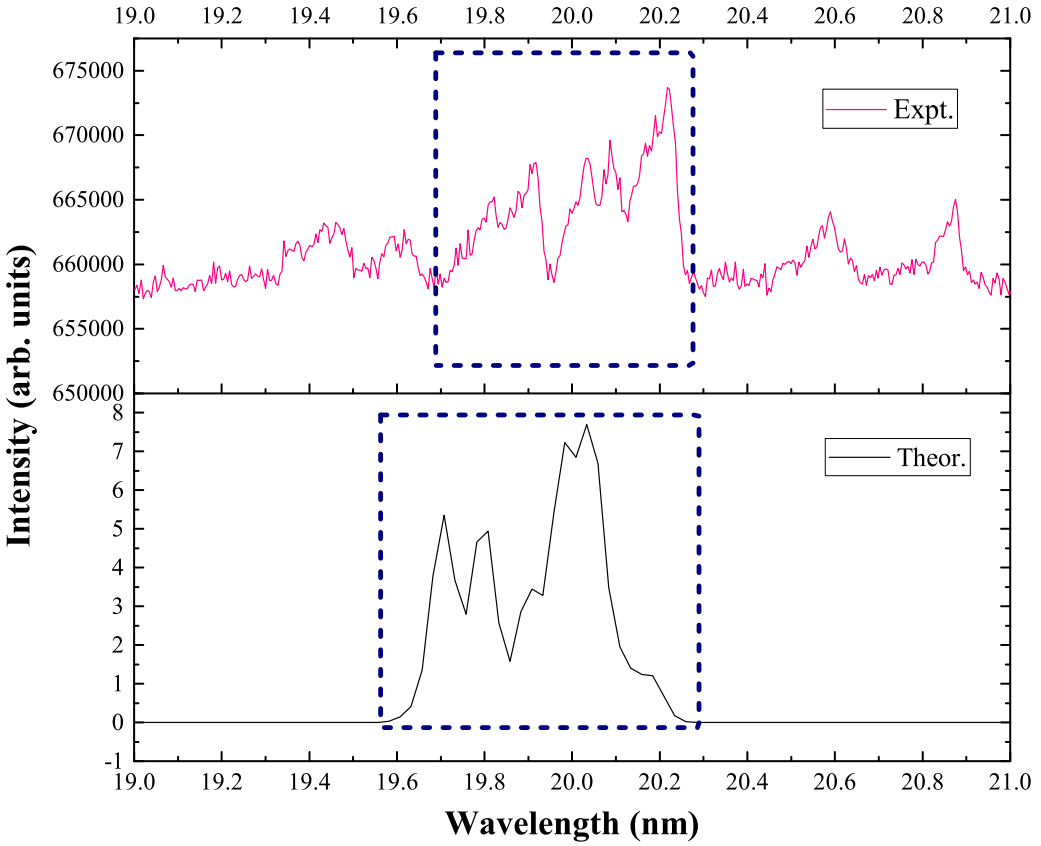

FIG. 7. Experimental and simulated spectra of W^{7+} ions in the EUV range 19–21 nm. Experimental spectra are obtained at a nominal electron-beam energy of 79 eV ($E_{corr} = 71.9$ eV) while the simulated spectra are obtained by CRM at electron-beam energy 70 eV and density $1.0 \times 10^{11}/\,\mathrm{cm}^3$ with energy spread 3.5 eV.

of the spectra is 2 h and the beam current is kept constant at 3 mA. The results are shown in Fig. 6 and the correction of electron-beam energy is shown in Table VI.

Different from spectra in visible range, lines in the EUV domain are mostly in the form of transition arrays, and thus difficult to identify when the resolution of the spectrometer is not high enough. It can be seen from Figs. 1 and 6 that the lines at 19.3–20.3 nm (61.1–64.2 eV) do not appear at the same time as the visible line at 574.49 nm when the nominal electron-beam energy setting 70 eV ($E_{\rm corr} = 60.0$ eV). After the electron-beam energy reaches 73 eV ($E_{\rm corr} = 63.9$ eV), they emerge gradually. As the electron-beam energy increases, the spectral lines in the transition array move toward lower wavelengths.

To explain this distinction between the visible and EUV spectra, the RCI method in FAC is used. A total of 1127 energy levels are obtained by considering configuration involving $4f^{13}5s^25p^6$, $4f^{13}5s^25p^55d^1$, $4f^{13}5s^25p^55f^1$, $4f^{13}5s^25p^56s^1$, $4f^{13}5s^25p^56p^1$, $4f^{13}5s^25p^56d^1$, $4f^{13}5s^15p^65d^1$, $4f^{13}5s^15p^65f^1$, $4f^{13}5s^15p^66s^1$, $4f^{13}5s^15p^66p^1$, $4f^{13}5s^15p^66d^1$, $4f^{14}5s^25p^5$, $4f^{14}5s^15p^6$, $4f^{12}5s^25p^65d^1$, $4f^{12}5s^25p^65f^1$, $4f^{12}5s^25p^66s^1$, $4f^{12}5s^25p^66p^1$, $4f^{12}5s^25p^66d^1$, $4f^{14}5s^25p^45d^1$, $4f^{14}5p^65d^1$, and $4f^{14}5s^15p^55d^1$. To identify these lines, spectra simulation was conducted by CRM under conditions of the electron energy 70 eV and density $1.0 \times 10^{11}/\mathrm{cm}^3$. The results are shown in Fig. 7 along with experimental results, and good agreement can be found.

According to the theoretical results, the transition array at 19.3–20.3 nm mainly arises from the transitions between the higher excited-state energy level (L209–L235) and the lower energy level (L0–L1). These include $5d$-$5p$, and $5d$-$4f$ $E1$ transitions. The detailed energy-level information is presented in Table VII.

The minimum nominal electron-beam energy, when lines in the visible and EUV ranges of W^{7+} ions occur, is 59 and 73 eV ($E_{\rm corr} = 54.9$ eV and $E_{\rm corr} = 63.9$ eV), respectively, which can be accounted for by the different mechanism of spectral line production based on our FAC calculation. After the electron-beam energy exceeds the ionization energy of W^{4+}, W^{7+} ions are generated by indirect ionization as mentioned above. As a result, the $M1$ line at 574.49 nm is observed at the 59-eV ($E_{\rm corr} = 54.9$ eV) electron-beam energy. However, the transition array at 20 nm comes from the $E1$ transitions from the higher-excited energy levels to the ground state of W^{7+}. Only if the corrected electron-beam energy $E_{\rm corr}$ exceeds the excitation energy of upper levels, approximately at 61.46 eV (see Tables VI and VII), can the direct impact excitation happen. Therefore, the transition array near 20.3 nm first appears as photon radiation from these excited states (see Fig. 6). As the electron-beam energy further increases up to 75 eV ($E_{\rm corr} = 65.7$ eV), the higher-excited levels are populated, giving rise to the appearance of a transition array near 19.9 nm.

TABLE VII. Related energy-level information. Here energy level represents the serial number in the calculated 1127 levels, and energy represents the relative energy compared to the ground state (0 eV) in W^{7+}.

Energy level	Configuration, J	Energy (eV)
L0	$(4f^{13}5s^25p^6)_{7/2}$	0.00
L1	$(4f^{13}5s^25p^6)_{5/2}$	2.26
L209	$(4f^{13}5s^25p^55d^1)_{5/2}$	61.46
L210	$(4f^{13}5s^25p^55d^1)_{7/2}$	61.65
L212	$(4f^{13}5s^25p^55d^1)_{9/2}$	61.86
L214	$(4f^{13}5s^25p^55d^1)_{5/2}$	62.06
L215	$(4f^{13}5s^25p^55d^1)_{9/2}$	62.07
L216	$(4f^{13}5s^25p^55d^1)_{7/2}$	62.30
L218	$(4f^{13}5s^25p^55d^1)_{7/2}$	62.62
L222	$(4f^{13}5s^25p^55d^1)_{9/2}$	62.93
L223	$(4f^{13}5s^25p^55d^1)_{5/2}$	63.14
L228	$(4f^{13}5s^25p^55d^1)_{7/2}$	63.69
L230	$(4f^{13}5s^25p^55d^1)_{5/2}$	63.92
L233	$(4f^{13}5s^25p^55d^1)_{7/2}$	64.57
L235	$(4f^{12}5s^25p^65d^1)_{3/2}$	64.92

V. CONCLUSIONS

The spectra of W^{7+} are measured in the visible and EUV ranges at SH-HtscEBIT under extremely low electron-beam-energy conditions. The 574.49(3) nm $M1$ line of W^{7+} is observed at the nominal electron-beam energy of 59 eV ($E_{\rm corr} = 54.9$ eV), which is below the ionization potential of W^{5+}. The multiconfiguration Dirac-Hartree-Fock calculation further confirms the identification of this line. A hypothesis of charge-state evolution from W^{5+} to W^{7+} is proposed, based on our theoretical studies on the energy levels of these charge states, to explain the appearance of W^{7+} spectra. Indirect ionization via stepwise excitations from the long-lived metastable states of lower-charge W ions plays a key role in the occurrence of W^{7+}. In addition, the EUV spectra at 75 eV ($E_{\rm corr} = 65.7$ eV) as well as the FAC calculations confirm that W^{7+} can be and is created via indirect ionization out of W^{5+}.

ACKNOWLEDGMENTS

This work was supported by the Chinese National Fusion Project for ITER No. 2015GB117000. One of the authors (Q.L.) thanks Dr. A. Kramida from the U.S. National Institute of Standards and Technology for his helpful explanation of the atomic data of W^{7+} in Ref. [48]. J.G.L. acknowledges support from National Natural Science Foundation of China (Grant No. 11874090).

[1] Y. Ralchenko, Plasma Fusion Res. **8**, 2503024 (2013).
[2] J. Clementson, P. Beiersdorfer, E. W. Magee, H. S. McLean, and R. D. Wood, J. Phys. B: At., Mol. Opt. Phys. **43**, 144009 (2010).
[3] V. Philipps, Phys. Scr. **T123**, 24 (2006).
[4] C. H. Skinner, Can. J. Phys. **86**, 285 (2008).
[5] V. Jonauskas, R. Kisielius, A. Kynienė, S. Kučas, and P. H. Norrington, Phys. Rev. A **81**, 012506 (2010).

[6] J. Clementson, P. Beiersdorfer, G. V Brown, and M. F. Gu, Phys. Scr. **81**, 015301 (2010).

[7] Y. Podpaly, J. Clementson, P. Beiersdorfer, J. Williamson, G. V. Brown, and M. F. Gu, Phys. Rev. A **80**, 052504 (2009).

[8] U. I. Safronova, A. S. Safronova, and P. Beiersdorfer, At. Data Nucl. Data Tables **95**, 751 (2009).

[9] C. Biedermann, R. Radtke, R. Seidel, and T. Pütterich, Phys. Scr. **T134**, 014026 (2009).

[10] J. Clementson and P. Beiersdorfer, Phys. Rev. A **81**, 052509 (2010).

[11] R. Neu, K. B. Fournier, D. Bolshukhin, and R. Dux, Phys. Scr. **T92**, 307 (2001).

[12] C. Biedermann, R. Radtke, J.-L. Schwob, P. Mandelbaum, R. Doron, T. Fuchs, and G. Fußmann, Phys. Scr. **T92**, 85 (2001).

[13] R. Radtke, C. Biedermann, P. Mandelbaum, and J. L. Schwob, J. Phys.: Conf. Ser. **58**, 113 (2007).

[14] Y. Ralchenko, I. N. Draganić, D. Osin, J. D. Gillaspy, and J. Reader, Phys. Rev. A **83**, 032517 (2011).

[15] H. Watanabe, N. Nakamura, D. Kato, H. A. Sakaue, and S. Ohtani, Can. J. Phys. **90**, 497 (2012).

[16] Y. Ralchenko, I. N. Draganic, J. N. Tan, J. D. Gillaspy, J. M. Pomeroy, J. Reader, U. Feldman, and G. E. Holland, J. Phys. B: At., Mol. Opt. Phys. **41**, 021003 (2008).

[17] Y.-J. Rhee and D.-H. Kwon, Int. J. Mass Spectrom. **271**, 45 (2008).

[18] A. Kramida, Can. J. Phys. **89**, 551 (2011).

[19] W. Li, Z. Shi, Y. Yang, J. Xiao, T. Brage, R. Hutton, and Y. Zou, Phys. Rev. A **91**, 062501 (2015).

[20] M. Li, M. Qiu, J. Xiao, K. Yao, T. Brage, R. Hutton, and Y. Zou, Phys. Scr. **91**, 105401 (2016).

[21] Z. Z. Zhao, M. L. Qiu, R. F. Zhao, W. X. Li, X. L. Guo, J. Xiao, C. Y. Chen, Y. Zou, and R. Hutton, J. Phys. B: At., Mol. Opt. Phys. **48**, 115004 (2015).

[22] Y. Kobayashi, K. Kubota, K. Omote, A. Komatsu, J. Sakoda, M. Minoshima, D. Kato, J. Li, H. A. Sakaue, I. Murakami, and N. Nakamura, Phys. Rev. A **92**, 022510 (2015).

[23] R. R. Kildiyarova, S. S. Churilov, Y. N. Joshi, and A. N. Ryabtsev, Phys. Scr. **53**, 454 (1996).

[24] F. G. Meijer, Physica (Amsterdam) **73**, 415 (1974).

[25] V. Kaufman and J. Sugar, J. Opt. Soc. Am. **66**, 1019 (1976).

[26] J. Sugar and V. Kaufman, J. Opt. Soc. Am. **69**, 141 (1979).

[27] J. Sugar and V. Kaufman, Phys. Rev. A **12**, 994 (1975).

[28] A. N. Ryabtsev, E. Y. Kononov, R. R. Kildiyarova, W.-Ü. L. Tchang-Brillet, and J.-F. Wyart, Opt. Spectrosc. **113**, 109 (2012).

[29] A. N. Ryabtsev, E. Y. Kononov, R. R. Kildiyarova, W.-Ü. L. Tchang-Brillet, and J.-F. Wyart, Phys. Scr. **87**, 045303 (2013).

[30] J.-F. Wyart, V. Kaufman, and J. Sugar, Phys. Scr. **23**, 1069 (1981).

[31] A. Kramida, Yu. Ralchenko, J. Reader, and NIST ASD Team, NIST Atomic Spectra Database (version 5.5.6), (National Institute of Standards and Technology, Gaithersburg, MD, 2018), https://physics.nist.gov/asd.

[32] J. Clementson, T. Lennartsson, P. Beiersdorfer, J. Clementson, T. Lennartsson, and P. Beiersdorfer, Atoms **3**, 407 (2015).

[33] M. Mita, H. Sakaue, D. Kato, I. Murakami, and N. Nakamura, Atoms **5**, 13 (2017).

[34] A. Windberger, F. Torretti, A. Borschevsky, A. Ryabtsev, S. Dobrodey, H. Bekker, E. Eliav, U. Kaldor, W. Ubachs, R. Hoekstra, J. R. Crespo López-Urrutia, and O. O. Versolato, Phys. Rev. A **94**, 012506 (2016).

[35] J. Sakoda, A. Komatsu, H. Kikuchi, and N. Nakamura, Phys. Scr. **T144**, 014011 (2011).

[36] M. L. Qiu, R. F. Zhao, X. L. Guo, Z. Z. Zhao, W. X. Li, S. Y. Du, J. Xiao, K. Yao, C. Y. Chen, R. Hutton, and Y. Zou, J. Phys. B: At., Mol. Opt. Phys. **47**, 175002 (2014).

[37] J. Xiao, R. Zhao, X. Jin, B. Tu, Y. Yang, D. Lu, R. Hutton, and Y. Zou, in *Proceedings of the 4th International Particle Accelerator Conference, IPAC2013, Shanghai, China* (JACoW, 2013), pp. 434–436.

[38] M. F. Gu, Can. J. Phys. **86**, 675 (2008).

[39] M. F. Gu, Phys. Rev. A **70**, 062704 (2004).

[40] P. Jönsson, G. Gaigalas, J. Bieroń, C. F. Fischer, and I. P. Grant, Comput. Phys. Commun. **184**, 2197 (2013).

[41] C. Froese Fischer, G. Gaigalas, P. Jönsson, and J. Bieroń, Comput. Phys. Commun. **237**, 184 (2019).

[42] Z. Shi, R. Zhao, W. Li, B. Tu, Y. Yang, J. Xiao, S. Huldt, R. Hutton, and Y. Zou, Rev. Sci. Instrum. **85**, 063110 (2014).

[43] M. L. Qiu, W. X. Li, Z. Z. Zhao, Y. Yang, J. Xiao, T. Brage, R. Hutton, and Y. Zou, J. Phys. B: At., Mol. Opt. Phys. **48**, 144029 (2015).

[44] X. Ding, J. Liu, F. Koike, I. Murakami, D. Kato, H. A. Sakaue, N. Nakamura, and C. Dong, Phys. Lett. A **380**, 874 (2016).

[45] B. S. Tu, M. C. Li, Q. F. Lu, Y. Yang, K. Yao, D. Lu, Y. Shen, C. Y. Chen, R. Hutton, Y. M. Zou, and J. Xiao, Phys. Lett. A **382**, 2673 (2018).

[46] B. Tu, Q. F. Lu, T. Cheng, M. C. Li, Y. Yang, K. Yao, Y. Shen, D. Lu, J. Xiao, R. Hutton, and Y. Zou, Phys. Plasmas **24**, 103507 (2017).

[47] J. C. Berengut, V. A. Dzuba, V. V. Flambaum, and A. Ong, Phys. Rev. Lett. **106**, 210802 (2011).

[48] A. E. Kramida and T. Shirai, At. Data Nucl. Data Tables **95**, 305 (2009).

[49] A. Ryabtsev, E. Kononov, R. Kildiyarova, W.-Ü. Tchang-Brillet, J.-F. Wyart, N. Champion, and C. Blaess, Atoms **3**, 273 (2015).

[50] M. S. Pindzola and D. C. Griffin, Phys. Rev. A **56**, 1654 (1997).